



Structural and mechanical evolution of *Tridacna gigas* during permineralization

Xue Hou^{a,b}, Hui Yu^{a,b}, Zhenhao Hou^b, Jianbao Li^{b,*}, Yongjun Chen^{b,**}, Lijie Luo^b, Xianzhi Chen^a, Wei Li^{a,b}, Huan Yang^{a,b}, Wei Zeng^c

^a State Key Laboratory of Marine Resource Utilization in South China Sea, College of Life Sciences & Pharmacy, Hainan University, Haikou, 570228, China

^b State Key Laboratory of Marine Resource Utilization in South China Sea, College of Materials Science & Engineering, Hainan University, Haikou, 570228, China

^c Center for Applied Biomechanics, University of Virginia, Charlottesville, VA, 22911, USA

ARTICLE INFO

Keywords:

Tridacna gigas
Mechanical properties
Microstructure
Permineralization

ABSTRACT

Mollusk shells have highly complex hierarchical structures and unique mechanical properties, which have been widely studied, especially in fresh shells. However, few studies have revealed differences in the structure-property correlations of shells during the permineralization process, which occurs after organism death. To better understand the effect of permineralization on the microstructure and mechanical properties of shells, this study investigated and compared the compositions, microstructures, and mechanical properties of *Tridacna gigas* and permineralized *J-Tridacna gigas*. The results showed that permineralized *J-Tridacna gigas* possessed coarsened aragonite minerals, less anisotropy and organic matter, and higher hardness and strength than *Tridacna gigas*. The toughening mechanisms of *Tridacna gigas*, including crack deflection, aragonite platelet pull-out, and mineral bridges, were discovered during Vickers hardness tests. Moreover, the permineralization mechanism comprised three main steps: organic matter dissolution, aragonite plate compaction, and recrystallization. This work further elaborates the permineralization mechanism, which can help increase the crystal size and improve the strength and hardness of materials. Moreover, this study provides valuable insights into the design of bioinspired advanced materials with outstanding hardness and strength.

1. Introduction

Highly mineralized biological composites synthesized in natural environmental conditions exhibit an excellent combination of stiffness, strength, and toughness. This outstanding mechanical performance benefits from the distinctive microstructures consisting of organic and mineral layers (Wegst et al., 2015; Aizenberg, 2005; Bechtle et al., 2010; Dunlop and Fratzl, 2013) and the viscoelastic properties of the organic-mineral nanostructure (Ji and Gao, 2004). The exceptional toughness properties of biological composites can be explained by different energy dissipating mechanisms, such as crack deflection, crack bridging, and multiple microcracking (Ji et al., 2014; Li and Ortiz, 2014; Wang et al., 2001).

Mollusk shells, which are typical biological composites, are hard and tough, and they support the internal soft structure and protect against predation (Addadi et al., 2006; Gannon et al., 2017; Pérez-Huerta et al., 2018; Schoeppler et al., 2018; Weiner, 2008). In general, the structure of

mollusk shells can be categorized into seven types: foliated, crossed-foliated, prismatic, nacreous, crossed-lamellar, complex crossed-lamellar, and homogeneous (Fleischli et al., 2008; Marin, 2012). Structural anisotropies exist in all these structures except for the homogeneous type. Nacreous structures are commonly found in shells that present two-dimensional anisotropy, whereas crossed-lamellar structures have three-dimensional anisotropies and are prevalent in bivalve and other classes. Structural anisotropies cause deformation and fracture mechanism differences, and they can be used to further determine the structure-property relations of mollusk shells. Many efforts have been made in the last few decades to study the mechanical performance, properties, and mechanisms of crossed-lamellar structures in fresh or live biological shells (Ji et al., 2015a; Lin et al., 2006; Meyers et al., 2008; Wang et al., 2001; Yang et al., 2011a,b,c). However, a limited number of studies have investigated the permineralization process after shell death.

Permineralization, which is initiated in mollusk shells after death, is

* Corresponding author.

** Corresponding author.

E-mail addresses: ljb555@hainu.edu.cn (J. Li), chenyj99@163.com (Y. Chen).

another important process in the early diagenesis of mollusk shells. During this process, the organic substance decays and disappears, after which the pores in the remaining organic tissue are filled with minerals (Pérez-Huerta et al., 2018; Ritter et al., 2017; Seiphoori et al., 2017; Toffolo et al., 2019). Some studies have investigated the behavior of and changes in mineral and organic compounds forming the skeleton of marine bivalves. Old bivalve shell skeletons preserved in aragonite are commonly used in carbonate geochemistry studies, such as paleotemperature or stratigraphic correlations, isotopic analyses to determine age, and paleoecological and paleoenvironmental studies based on the trace elements and isotopic contents of carbonate skeletal remains (Perrin and Smith, 2007). Nevertheless, few works have systematically studied the changes in the microstructure and mechanical properties of mollusk shells (*Tridacna gigas*) during permineralization. In particular, a precise understanding of the permineralization process of *Tridacna gigas* could provide insights into the design of multilayered bioinspired materials with exceptional properties.

In this work, the phase composition, hierarchical microstructure and nanostructure, mechanical properties, and their correlation in J-*Tridacna gigas* (permineralized) were investigated and compared with those in *Tridacna gigas*. The results demonstrated the impact of organic matter reduction, coarsening, and recrystallization of inorganic components on micro- and nanostructural changes, which were correlated with the permineralization processes. The mechanism of microstructural change and the resulting high strength and hardness were explained. Moreover, the toughening mechanisms of *Tridacna gigas*, including crack deflection, aragonite platelet pull-out, and mineral bridges, were discovered. This study provides knowledge on structure-property correlation during the permineralization process of *Tridacna gigas* and offers new insights into the design of bioinspired advanced structural materials for use in the aerospace industry, knives, and body armor.

1.1. Sample acquisition and selection

Dead *Tridacna gigas* (65 cm in height, 42 cm in width, and 11 cm in thickness) from the bottom of the South China Sea were obtained from local fishermen. The samples were prepared from two regions on the same *Tridacna gigas*: a highly transparent permineralized region (jade) in the middle of the shell and a less transparent region 50 mm from the lower edge of the shell. For the polished samples, which were 1 mm in thickness, their transmittances were 72% and 31%, respectively.

1.2. Composition analysis

Powders from the middle layers of the normal and J-*Tridacna gigas* were obtained using a three-head grinding machine (XPM – Φ120 × 3, Wu Tan, China). The sieve size was between 200 mesh and 400 mesh, and the particle size distribution ranged from 40 μm to 80 μm.

The inorganic phase compositions of jade and normal *Tridacna gigas* were identified using an X-ray diffraction analysis system (D8 ADVANCE, Bruker, Germany). The acceleration voltage was 40 kV, and the current was 30 mA. The step size, scan rate and 2θ range were set to 0.02, 0.04°/s and 10–60°, respectively.

Thermogravimetric analysis (TGA) and differential scanning calorimetry (DSC) were performed on powder samples using a simultaneous thermal analyzer (Netzsch STA 449F3, Netzsch, Germany). The powder samples were heated at a rate of 10 °C/min from room temperature to 900 °C under a nitrogen environment.

The volume density and apparent porosity of the *Tridacna gigas* were calculated according to Archimedes' principle.

1.3. Microstructure characterization

The through-thickness cross sections were created perpendicular to the growth line on the jade and normal *Tridacna gigas* using a low-speed diamond wire saw (STX-202A, Shenyang Kejing, China). The cross-

sectional specimens were immersed in 0.1% hydrochloric acid for 15 s (Xilong, China) before being thoroughly washed with deionized water and air dried. The microscopic morphology of the *Tridacna gigas* sample surface was observed via scanning electron microscopy (SEM; S-4800, Hitachi, Japan) after sputter coating the sample with a 20 nm gold film. For the SEM observations, the acceleration voltage was 10 kV, and the current was 10 mA.

1.4. Mechanical testing

All specimens for mechanical testing were prepared using a low-speed diamond wire saw. Each mechanical testing method was performed on ten specimens per sample type along each direction in the study (Fig. 1).

The flexural strength of the jade and normal *Tridacna gigas* specimens was measured with a universal testing machine (10 kN load cell, AGS-10KNG, Japan) through three-point bending tests. The dimensions of the specimens were 3 mm in height, 4 mm in width, and 36 mm in length. The flexural span was 30 mm, and the bending rate was 0.5 mm/min until sample failure. The flexural strength was defined as the highest stress at the beam surface before sample failure.

Uniaxial compression testing was performed with the same machine and load cell. The specimen dimensions were 5 mm in width, 5 mm in thickness, and 12 mm in height. The displacement rate during compression testing was 0.5 mm/min until a sudden drop in load occurred due to fracture. The compressive strength was defined as the highest stress on the stress-strain curve before the first sudden drop in stress occurred.

The fracture toughness was obtained using the single-edge notched beam method. The dimensions of the beam were 4 mm in thickness, 2 mm in width, and 25 mm in length. A triangular notch that was 2 mm in width, 2 mm in length, and 2 mm in depth was created at the center of the 2 mm × 25 mm surface. The span of the fracture toughness test was 16 mm, and a displacement rate of 0.05 mm/min was applied on the sample. The fracture toughness was calculated by integrating the area under the stress-strain curve up to the point of fracture.

The microhardness was measured with a microhardness tester (HVS-1000Z, China) using a Vickers three-sided pyramid diamond indenter. The tests were carried out on each surface (orientations A, B, and C) under a load of 19.6 N, which was held for 15 s (Fig. 1).

The elastic modulus and nanohardness were tested using a Bruker nanoindentation device equipped with a Berkovich pyramidal indenter (TI 980, Bruker, Germany). A load of 200 mN was applied up to maximum load in 15 s. For each sample, at least 20 indentations were carried out in the form of a group of 5 points in 4 different positions. Each two indentations were spaced by 100 μm to avoid the influences of residual stresses.

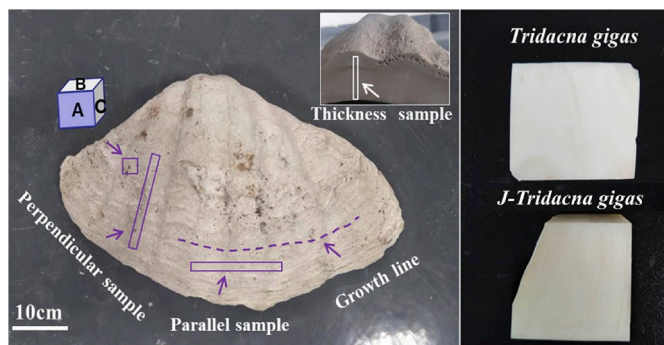


Fig. 1. Appearance and sample orientation on *Tridacna gigas*. The cutting direction and positions of the test pieces are marked with blue boxes. A: Outer/inner surface. B: Parallel cross section (parallel to the growth line, through the thickness). C: Perpendicular cross section (perpendicular to the growth line, through the thickness).

2. Results

2.1. Compositions and phases

TGA revealed a distinct difference in the organic matter percentage between jade and normal *Tridacna gigas*. Upon heating, the main weight loss in the samples occurred between 550 °C and 780 °C (Fig. 2a) due to the decomposition of calcium carbonate. The weight loss in J-*Tridacna gigas* (43.73%) was slightly lower than that in *Tridacna gigas* (44.85%) at 25 °C–900 °C (Fig. 2a).

The weight of the sample decreased in two steps before the decomposition of calcium carbonate. In Fig. 2b, two steps can be found in the temperature range before 680 °C. The weight loss was 0.36% for *Tridacna gigas* in the first step (from room temperature to 200 °C). In the second step (from 200 °C to 550 °C), the weight loss in J-*Tridacna gigas* (0.59%) was 64.5% less than that in *Tridacna gigas* (1.66%).

The endothermic peak on the differential thermal analysis (DTA; Fig. 2c) and DSC curves (Fig. 2d) of J-*Tridacna gigas* (763 °C) was slightly higher than that of *Tridacna gigas* (759 °C).

The volume density (Fig. 3) of J-*Tridacna gigas* was 2.89 g/cm³, which was 0.03 g/cm³ higher than that of *Tridacna gigas* (2.86 g/cm³). The *Tridacna gigas* absorbed much more water (0.82%) than the J-*Tridacna gigas* (0.04%).

The 2θ values, the intensities of the labeled peaks, and the corresponding d-spacings were plotted on X-ray diffractograms (Fig. 4). Although the peak intensities were slightly different, the peak positions were nearly identical, indicating that aragonite CaCO₃ was the dominant phase in both jade and normal *Tridacna gigas*. Aragonite CaCO₃ has an orthorhombic lattice with the following lattice parameters: $a = 4.962 \text{ \AA}$, $b = 7.968 \text{ \AA}$, and $c = 5.744 \text{ \AA}$ (JCPDS Card No. 41-7457; space group: Pmcn).

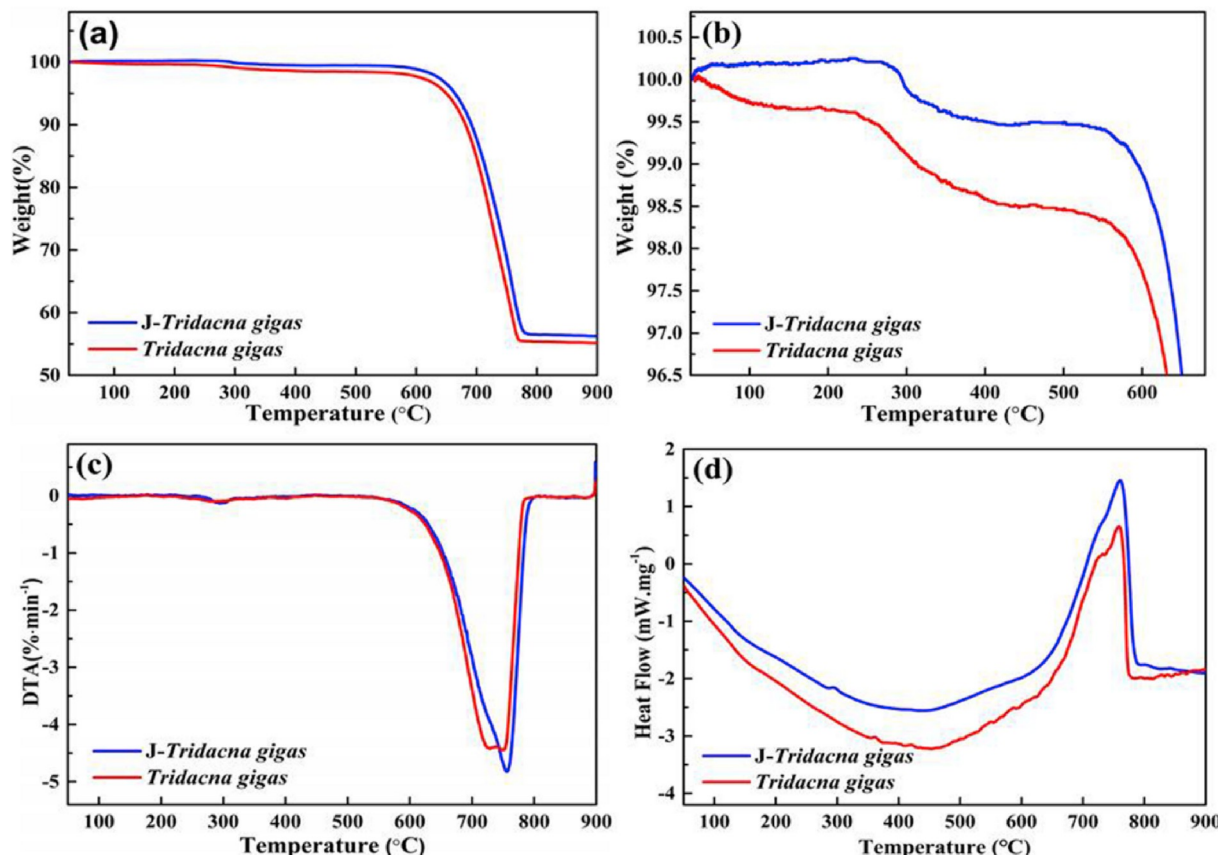


Fig. 2. Evolution of properties: (a) TG curves of jade and normal *Tridacna gigas* powders. (b) Magnified view of the TG curves below 700 °C. (c) DTA curves of jade and normal *Tridacna gigas* powders. (d) DSC curves.

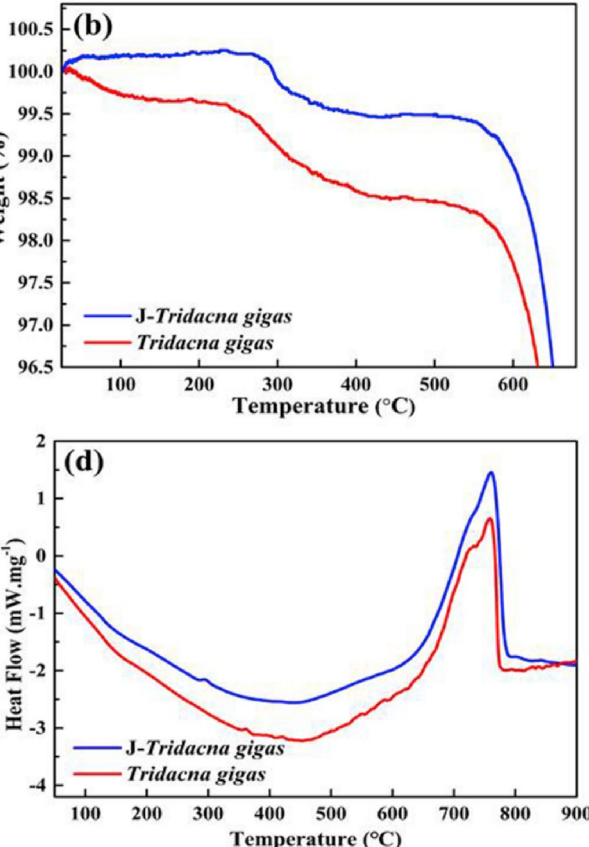


Fig. 3. Volume density and apparent porosity of jade and normal *Tridacna gigas*.

2.2. Microstructures of J-*Tridacna gigas*

The microstructures of J-*Tridacna gigas* were observed using SEM. Three orders of lamellae were observed forming a hierarchically crossed-lamellar structure, including first-order lamellae, second-order lamellae, third-order lamellae and nanograins, as shown in Fig. 5. The sheet-like first-order lamellae (Fig. 5e) were stacked parallel to each other to form a macrolayer, similar to the distinctive structure of a *Cymbiola nobilis* shell. Nanoscale aragonite rods (third-order lamellae) were highly aligned and closely packed (Fig. 5a and f), and their lengths

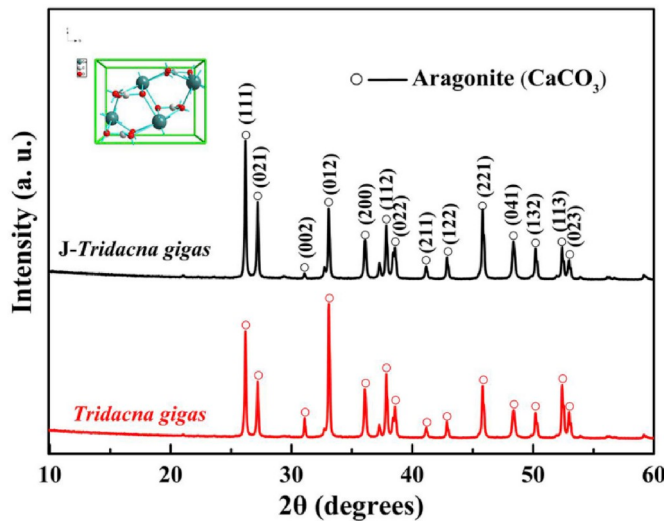


Fig. 4. X-ray diffraction patterns of jade and normal *Tridacna gigas*.

and thicknesses were 15.67 ± 2.16 and 1.27 ± 0.44 μm , respectively. Nanorods with similar long axes were assembled into platelets with parallel long axes, which become second-order lamellae with parallel distributions; their thickness was approximately 19.68 ± 3.14 μm (Fig. 5c). The second-order lamellae were then packed together into first-order lamellae, which were approximately 63.03 ± 16.85 μm in thickness (Fig. 5e), by the adhesion between the largest parallel surfaces. In addition, nanograins with a diameter of approximately 84.06 ± 15.67 nm were unevenly distributed on the surface of the aragonite rods (Fig. 5a and d). Fig. 5b shows a schematic of the hierarchical lamellar structure of J-*Tridacna gigas*.

The size of the aragonite platelets in J-*Tridacna gigas* (1.27 ± 0.44 μm) was approximately twice as large as that in *Tridacna gigas* (0.60 ± 0.55 μm), as shown in Fig. 7. The nanogranules on the surface of J-*Tridacna gigas* were found to be smaller in size, lower in height, and smoother than those on the surface of *Tridacna gigas* (Fig. 6c and d).

Fig. 8a and b shows the polished surfaces (surface A) of the normal and jade *Tridacna gigas*, respectively. Compared with *Tridacna gigas*, J-

Tridacna gigas had smaller and fewer holes, which was consistent with the low apparent porosity results in Fig. 3. Under the action of deep sea hydrostatic pressure, the aragonite platelets of J-*Tridacna gigas* were compacted, as shown in Fig. 8c. The fusion of the aragonite platelets results in coarsening of the crystal size and recrystallization, as indicated by the arrows in Fig. 8d.

2.3. Mechanical properties

To explore the differences in the mechanical properties of jade and normal *Tridacna gigas*, mechanical tests and Weibull distributions were conducted in the A, B, and C orientations of the samples. The properties tested included flexural strength, compressive strength, fracture toughness and Vickers hardness, which are compared in Fig. 9.

The flexural strength results (50% of the probability of failure) of the jade and normal *Tridacna gigas* samples showed similar trends. In both samples, the parallel direction exhibited the highest strength, whereas the perpendicular direction had the lowest strength. The J-*Tridacna gigas* had a lower variation in strength (from 50.37 MPa to 61.42 MPa) than normal *Tridacna gigas* (36.69 MPa– 108.89 MPa) in the three orientations. In *Tridacna gigas*, the flexural strength of the parallel samples was nearly 200% higher than that of the perpendicular samples. Conversely, in J-*Tridacna gigas*, the samples exhibited similar flexural strength in all directions.

The compressive strength results were obtained from ten specimens of jade and normal *Tridacna gigas* in the direction perpendicular to the A, B, and C planes. The compressive strength results of J-*Tridacna gigas* in each orientation (50% of the probability of failure) were 138.43 , 120.44 , and 103.62 MPa, which were significantly higher than those of *Tridacna gigas* (87.46 , 114.72 , and 90.83 MPa, respectively).

The fracture toughness of the jade and normal *Tridacna gigas* exhibited similar trends to their bending strength. The J-*Tridacna gigas* had a lower variation in toughness (from 0.99 ± 0.07 MPa $\text{m}^{1/2}$ to 1.16 ± 0.03 MPa $\text{m}^{1/2}$) than *Tridacna gigas* (0.88 ± 0.07 MPa $\text{m}^{1/2}$ to 1.95 ± 0.40 MPa $\text{m}^{1/2}$); the toughness variation in *Tridacna gigas* was approximately 6 times that in J-*Tridacna gigas*.

The Vickers hardness values of J-*Tridacna gigas* were higher than those of *Tridacna gigas* in the three orientations (Fig. 9f). The measured hardness values of J-*Tridacna gigas* in the three orientations were 3.51 ± 0.16 , 3.27 ± 0.23 , and 3.22 ± 0.22 GPa. In contrast, the hardness values

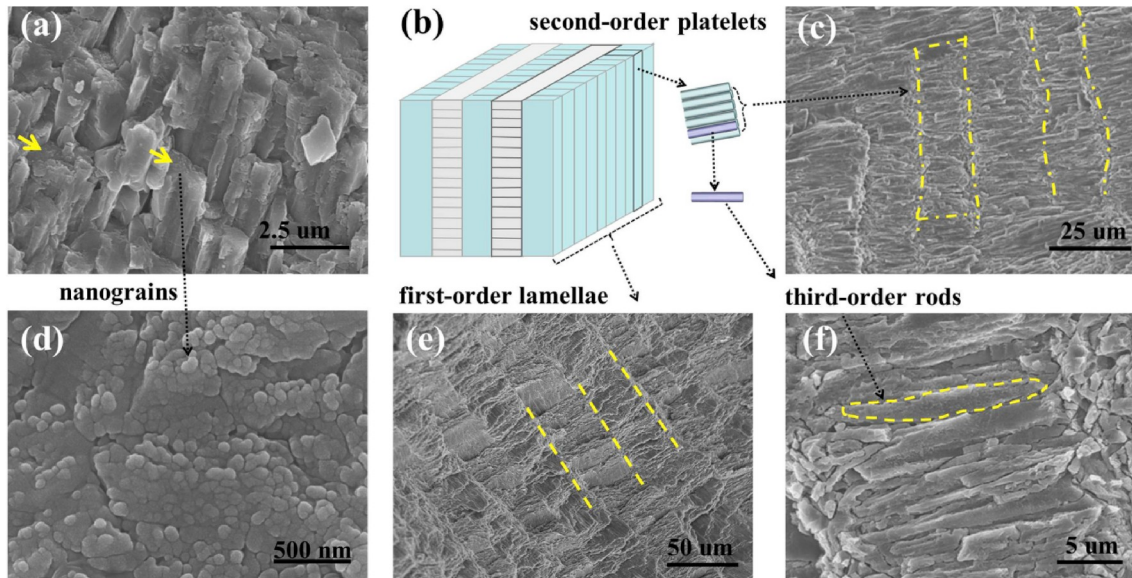


Fig. 5. Microstructure of J-*Tridacna gigas* observed by SEM. (b) Schematic of the hierarchical lamellar structure. Nanorods (third-order lamellae, shown in a and f) assembled into platelets (second-order lamellae, shown in c), which then stack into a larger layered structure (first-order lamellae, shown in e). (d) Nanograins on the surface of the nanorods (third-order lamellae, shown in a).

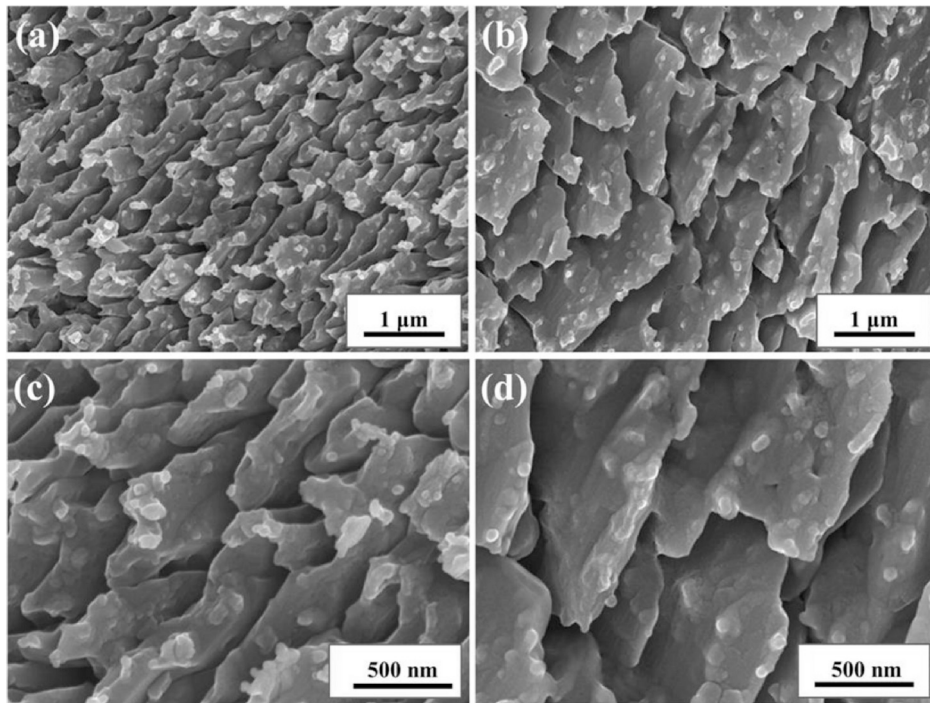


Fig. 6. SEM micrographs of jade and normal *Tridacna gigas* etched in 0.1% HCl for 15 s. (a) Low-magnification image of *Tridacna gigas*. (b) Low-magnification image of J-*Tridacna gigas*. (c) Higher magnification image of *Tridacna gigas*. (d) Higher magnification image of J-*Tridacna gigas*.

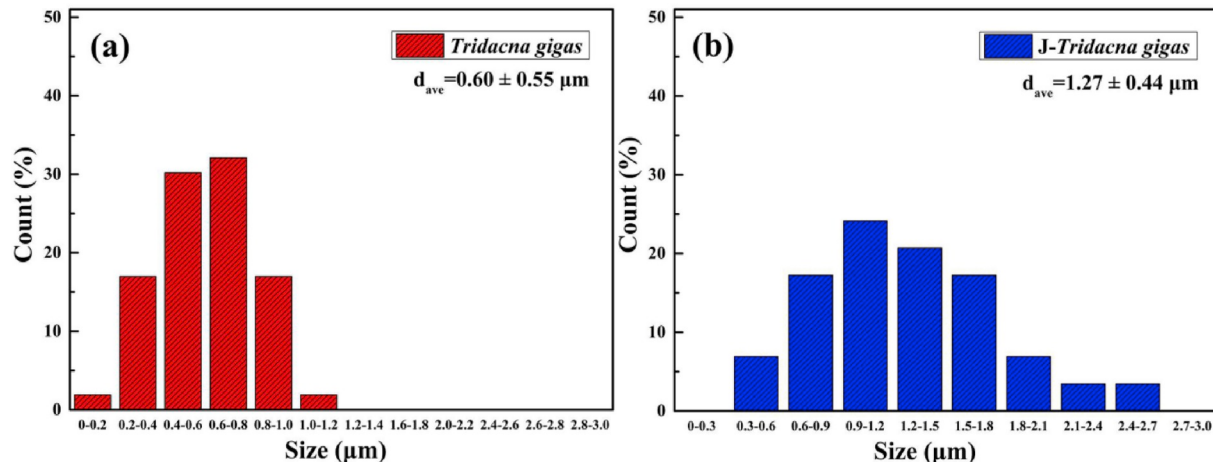


Fig. 7. Aragonite platelet size distribution of (a) normal and (b) jade *Tridacna gigas*.

of *Tridacna gigas* were 0.80–1.00 GPa lower (2.51 ± 0.40 , 2.58 ± 0.25 , and 2.42 ± 0.43 GPa, respectively).

The nanohardness and Young's modulus of jade and normal *Tridacna gigas* exhibited similar trends to their microhardness (Fig. 10c); however, the nanohardness was higher than the microhardness. The ratio of nanoindentation hardness to Young's modulus (H/E) of J-*Tridacna gigas* was higher than that of *Tridacna gigas* in orientations A and C, whereas this ratio was similar between the two samples in orientation B. The results of the nanohardness and H/E ratio of the two samples are presented in Table 1. Moreover, the load-depth curves were obtained under a constant force of 200 mN (Fig. 10a and b).

2.4. Permineralization and fracture mechanism

Fig. 11 shows the fracture surfaces of jade and normal *Tridacna gigas* samples investigated via SEM. The morphologies of all three fracture

surfaces of J-*Tridacna gigas* were similar (smooth fracture surfaces), indicating lower anisotropy than *Tridacna gigas*. In comparison with J-*Tridacna gigas*, *Tridacna gigas* had finer-textured surface fractures and had more obvious lamellar patterns in the parallel, perpendicular, and thickness samples. The sharp breaks and holes created by the first-order lamellar fracture and pull-out are indicated by the arrows in Fig. 11d and the circles in Fig. 11e. In addition, the lamellar texture of the fractured surface is indicated by the arrow and curved lines in Fig. 11f.

The yellow outlines reflecting the size of the building blocks are shown in Fig. 12. Clearly, the size of the aragonite building blocks in J-*Tridacna gigas* was significantly larger than that in *Tridacna gigas*, which was consistent in the three different orientations. In addition, the aragonite platelets in J-*Tridacna gigas* were denser than those in *Tridacna gigas*, which agreed with the lower apparent porosity of J-*Tridacna gigas* shown in Fig. 3.

Fig. 13 shows the failure crack propagation morphologies of jade and

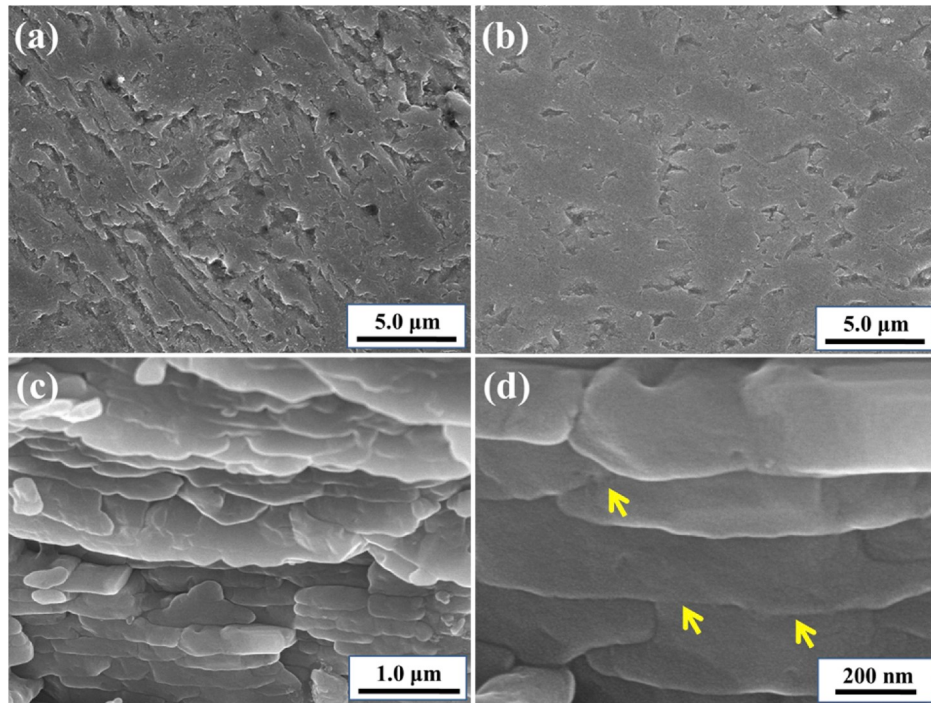


Fig. 8. SEM micrographs. (a, b) Polished surfaces of samples (surface A) of normal and jade *Tridacna gigas*. (c) Fracture surface of J-*Tridacna gigas* aragonite rods compacted under hydrostatic pressure. (d) Magnified view of compacted aragonite rods and aragonite rod fusion in J-*Tridacna gigas*.

normal *Tridacna gigas* using a Vickers hardness tester. Compared with *Tridacna gigas* (Fig. 13a), J-*Tridacna gigas* exhibited more severe damage, as featured by the large fractured blocks around the indenter, the large crushed zone, and the straight cracks (Fig. 13b). In addition, the hierarchical laminated structure of J-*Tridacna gigas* led to unique toughening mechanisms, including crack deflection, zig-zag paths, mineral bridges, and aragonite platelet pull-out (Fig. 13c–f, respectively), which enhanced the crack propagation damage resistance.

3. Discussion

3.1. Evolution of composition and phase during permineralization

The first step in the two-step weight loss during TGA, which was exhibited by the normal *Tridacna gigas*, occurred due to the evaporation of unbonded water and small acid molecules (Agbaje et al., 2017a,b; Lu et al., 2018); during this step, the weight of J-*Tridacna gigas* remained constant. The second step was ascribed to the decomposition of organic components. The differences indicated that the J-*Tridacna gigas* not only contains less organic content than *Tridacna gigas* but also holds significantly less humidity in its very limited organic content after permineralization. The density and apparent porosity measurements provided another set of evidence of similar phenomena. The high density, low organic content (approximately half), and very low moisture content in J-*Tridacna gigas* should influence the corresponding brittle mechanical properties.

Both jade and normal *Tridacna gigas* were nearly exclusively composed of aragonite, similar to the results reported for many other types of bivalve mollusk shells (Pokroy et al., 2009; Rodriguez et al., 2017; Zhang and Xu, 2013). During permineralization, although the size of crystals increased dramatically, as observed in the SEM images, the phase change of calcium carbonate was not evident. The aragonite calcium carbonate became calcite after a phase change at approximately 500 °C (Agbaje et al., 2017a,b). The decomposition temperature of calcium carbonate was similar to that in previous results (600–800 °C) (Rodriguez et al., 2017). A low decomposition temperature in *Tridacna*

gigas was also found by Mohamed et al. (2012), who reported that the thermal degradation temperature of the biological calcite phase (727–773 °C) was lower than that of geological calcite (850 °C). In addition to the possibility that the presence of organic impurities promoted the decomposition of calcium carbonate, the low decomposition temperature was likely due to the effect of the smaller crystal size in the nanoscale.

3.2. Decreasing anisotropy and increasing hardness during permineralization

The microhardness, nanohardness, compressive strength, bending strength, and fracture morphologies of the two samples were found to be different in the three directions, wherein this mechanical anisotropy was dictated by the microstructural anisotropy.

The microhardness of J-*Tridacna gigas* (3.51 ± 0.16 , 3.27 ± 0.23 , and 3.22 ± 0.22 GPa) was similar to the hardness of geological aragonite (3.26 GPa) (Mu et al., 2018), indicating a very limited amount of residual organic compounds. In comparison, the microhardness of *Tridacna gigas* was approximately 0.8–1.00 GPa lower than that of J-*Tridacna gigas*, which was also observed in *Perna canaliculus* shells (2.55 GPa) and mother of pearl (2.3 GPa). In general, the compressive strength of J-*Tridacna gigas* was higher than that of *Tridacna gigas*. The difference in hardness and compressive strength between jade and normal *Tridacna gigas* may be due to the content of organic matter, which consisted mainly of polysaccharides and proteins (Addadi et al., 2006). When the soft organic phase existed, the deformation during indentation occurred predominately in the soft phase, resulting in an average hardness of the organic-inorganic composites. Given the linear nature of elastic deformation and the intimate bonding between organic matter and aragonite platelets, the increase in Young's modulus can be calculated by the rule of mixtures:

$$E = E_1 v_1 + E_2 v_2 \quad (1)$$

where E is the composite modulus, E_1 is the organic matter modulus, v_1 is the organic matter volume fraction, E_2 is the aragonite platelet

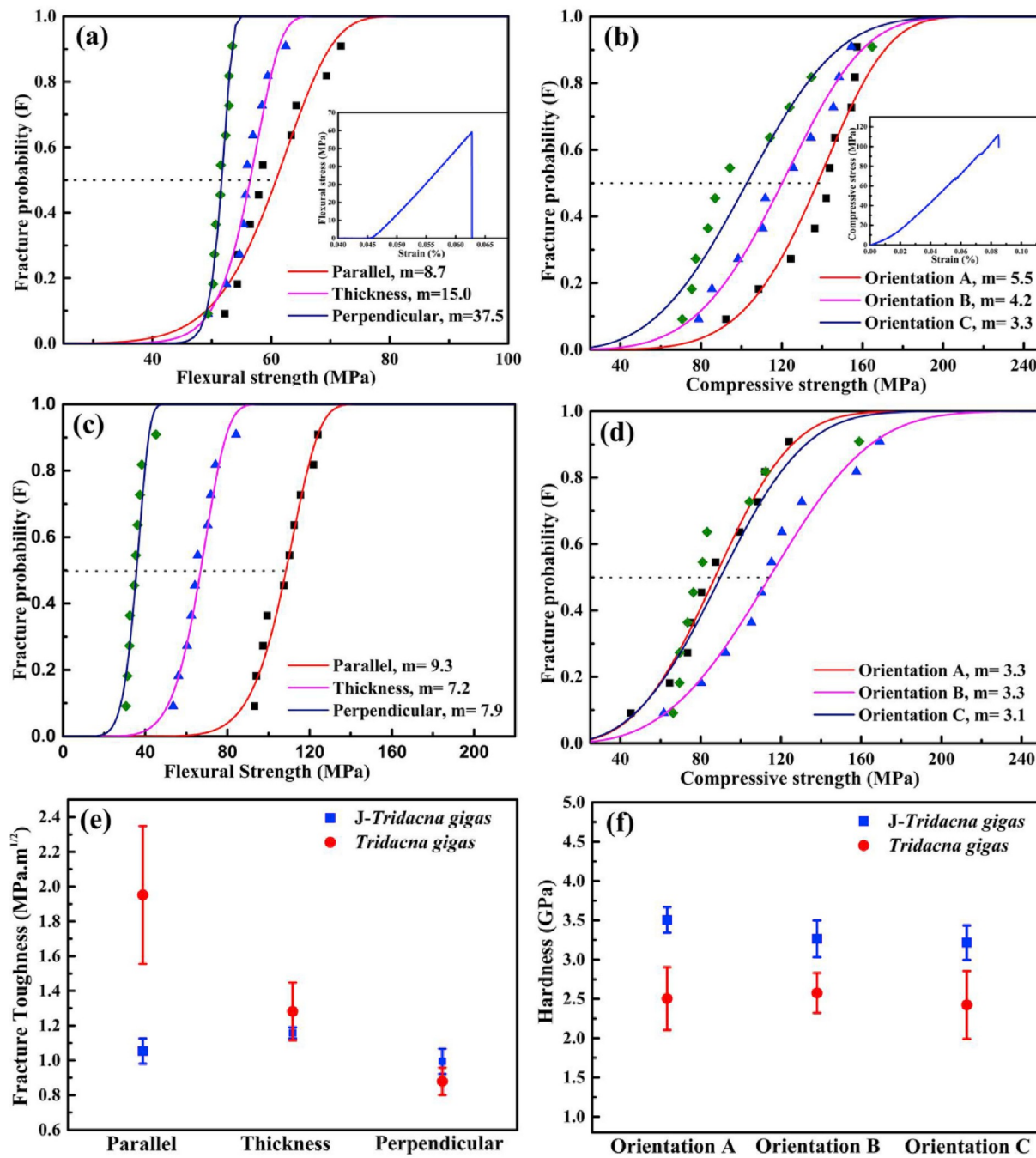


Fig. 9. Mechanical properties of jade and normal *Tridacna gigas* in three orientations: Weibull fit of (a) jade and (c) normal *Tridacna gigas* in the flexural test, Weibull fit of (b) jade and (d) normal *Tridacna gigas* in the compression test, m is the Weibull modulus, (e) results of the fracture toughness tests and (f) results of the hardness tests. The stress-strain plots of the flexural and compression specimens obtained from J-*Tridacna gigas* were inserted in (a) and (b), respectively.

modulus, and ν_2 is the aragonite platelet volume fraction (Zhang et al., 2019). As the organic matter content decreased, the crystal structure of J-*Tridacna gigas* was rearranged, resulting in stronger stability and improved properties (Jiao et al., 2016b).

The hardness and compressive strength of both samples exhibited similar trends in terms of anisotropy in the same sample type; however, the compressive strength of J-*Tridacna gigas* was significantly higher than that of *Tridacna gigas*. The strength contribution can be expressed as follows:

$$\sigma = \sigma_o \exp(-bp) \quad (2)$$

where σ is the strength, σ_o is the theoretical strength, b depends on the

materials, and p is porosity. As the porosity decreased, the compressive strength of J-*Tridacna gigas* improved. The compressive strength anisotropies with respect to the loading along the three orientations agreed well with the observations of Yang et al. (Yang et al., 2011a,b,c) in Araguaiá bivalve shells, for which the compressive strength was 347 MPa parallel to the shell surface and 567 MPa perpendicular to the shell surface. The anisotropy of hardness and compressive strength in the same samples was likely generated by similar mechanisms. When the force was applied perpendicular to the sample surface, both phases were connected in series, and the weaker organic phase determined the compressive strength of the samples. On the other hand, when the force was applied parallel to the sample surface, during which the two phases were subjected to the same stress, the stronger phase can sustain a

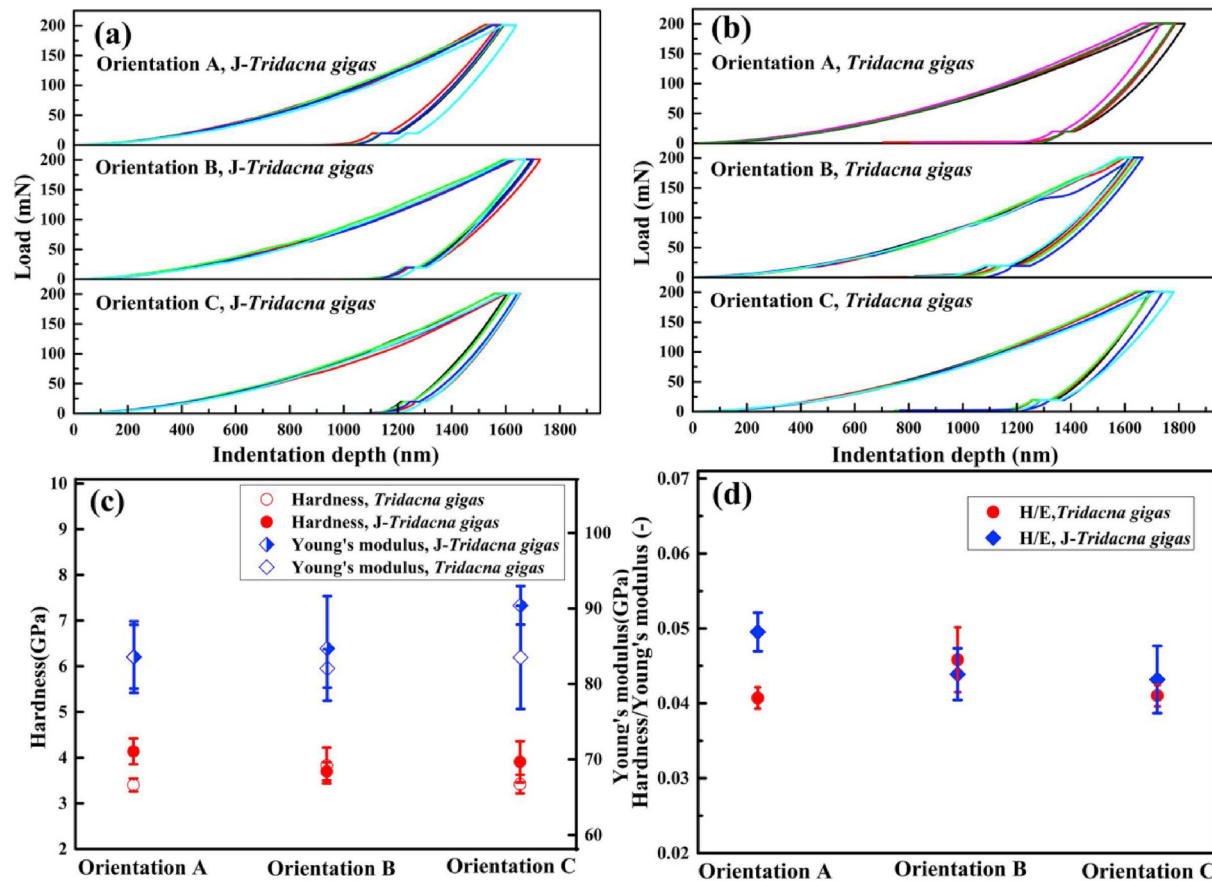


Fig. 10. Nanoindentation curves of jade and normal *Tridacna gigas*. (a, b) Load-depth curves. (c) Nanohardness and Young's modulus. (d) *H/E* ratio.

higher level of force than the weaker phase, and the samples were consequently stronger (Jiao et al., 2016a).

The fracture surfaces of *Tridacna gigas* under different bending directions were consistent with the findings published by Ji et al. (2017), who observed that the fracture surface morphology was rough in perpendicular samples and relatively smooth in parallel samples. This phenomenon may be attributed to the fact that the microstructures of the samples were composed of layered structures with hierarchically aligned aragonite platelets (lamellae) of calcium carbonate, which were “glued” together by an organic substance (Bechtle et al., 2010; Mishra and Kandasubramanian, 2018). Fracturing in the layer accounts for a larger amount of dissipated energy when the load is applied perpendicular to the surface of the aragonite platelets than when loaded parallel to the aragonite platelets. Cracking in the “weak” layer only absorbs a small amount of energy. The microstructures of the fracture surfaces further explain why the parallel samples exhibit higher bending strength than the perpendicular or thick samples. The bending strength significantly varied in each orientation among different shells. Ji et al. (2015b) performed three-point bending measurements on a single layer of *Scaevola broughtonii* shell along orthogonal orientations. They found that the bending strength along the stacked orientation was significantly lower (approximately 60%) than that along the tiled orientation.

Compared with J-Tridacna gigas, normal *Tridacna gigas* exhibited higher bending strength and fracture toughness, which was likely due to the higher fraction of organic matter and porosity in the latter (Romana et al., 2013). In addition, the organic matter loss and recrystallization during permineralization led to a decrease in the anisotropy of J-Tridacna gigas. The decomposition of organic matter and coarsening of crystals during permineralization increased the homogeneity of the structure, so that the properties of anisotropy became indistinct in J-Tridacna gigas along the three orientations.

To better understand the influence of permineralization on the mechanical properties of *Tridacna gigas*, a nanoindentation test (Fig. 9) was applied in the three directions, and the results were compared with those from the Vickers hardness test. Clearly, the nanoindentation hardness of J-Tridacna gigas (3.70 ± 0.20 GPa to 4.14 ± 0.28 GPa) was higher than that of *Tridacna gigas* (3.42 ± 0.20 GPa to 3.83 ± 0.39 GPa). However, the nanohardness value was higher than that of the microhardness, which was consistent with the findings of Boufala et al. and Labonte et al. (Boufala et al., 2019; Labonte et al., 2017), who reported that the nanohardness values in *Pecten maximus*, *Meretrix lusoria*, and *Charonia lampas* were significantly higher than the microhardness values. This phenomenon may be caused by the small indenter and low loads applied during the nanoindentation test, which results in the nanohardness value becoming more sensitive than the microhardness value (Katti et al., 2006). The Young's modulus of *Tridacna gigas* was used to evaluate the resistance to elastic deformation, as shown in Table 1. The variation range of Young's modulus was small for both samples (82.06 ± 2.55 GPa to 84.69 ± 6.93 GPa) except for orientation C in J-Tridacna gigas, indicating that the organic matter had a minor impact on Young's modulus when tested at the nanoscale. This phenomenon may be attributed to the low organic matter content in the two samples, which results in the nanoindentation test loading force being applied on the mineral phase rather than on the organic matter, such as orientation C in J-Tridacna gigas. The *H/E* ratio can be used to evaluate the damage resistance and fracture toughness of shell materials. A low *H/E* ratio indicates a high fracture toughness (Mu et al., 2018; Fleischli et al., 2008). From Table 1, the *H/E* ratios of J-Tridacna gigas were higher than those of *Tridacna gigas* in orientations A and C, whereas the ratios were similar in orientation B. Thus, J-Tridacna gigas had a lower fracture toughness than normal *Tridacna gigas*. Labonte et al. (Labonte et al., 2017) reported that the *H/E* ratio of many biological materials is nearly

Table 1

Values of hardness (H) and Young's modulus (E) of various mollusks measured by nanoindentation.

Species	Class	H (GPa)	E (GPa)	H/E	Ref.
<i>J-Tridacna gigas</i>	B	4.14 ± 0.28 ^{Mid, T}	83.56 ± 4.74 ^{Mid, T}	0.049	This work
		3.70 ± 0.20 ^{Mid, PA}	84.69 ± 6.93 ^{Mid, PA}	0.044	
		3.91 ± 0.45 ^{Mid, PE}	90.39 ± 2.55 ^{Mid, PE}	0.043	
		3.40 ± 0.14 ^{Mid, T}	83.60 ± 4.21 ^{Mid, T}	0.041	
		3.83 ± 0.39 ^{Mid, PA}	82.06 ± 2.55 ^{Mid, PA}	0.046	
<i>Tridacna gigas</i>	B	3.42 ± 0.20 ^{Mid, PE}	83.52 ± 6.83 ^{Mid, PE}	0.041	
		4.33 ± 0.12 ^{In, P}	80.61 ± 1.26 ^{In, P}	0.054	
		2.34 ± 0.26 ^{Mid, P}	51.45 ± 3.25 ^{Mid, P}	0.046	
		2.33 ± 0.32 ^{Out, P}	52.15 ± 4.35 ^{Out, P}	0.045	
		4.69 ± 0.07 ^{In, T}	85.95 ± 1.48 ^{In, T}	0.054	
<i>Manila clam</i>	B	3.04 ± 0.20 ^{Mid, T}	59.93 ± 1.72 ^{Mid, T}	0.051	Mu et al. (2018)
		3.35 ± 0.38 ^{Out, T}	61.51 ± 4.10 ^{Out, T}	0.054	
		2.87 ± 0.15 ^{Out}	56.24 ± 1.16 ^{Out}	0.051	
		3.64 ± 0.80 ^{Mid}	64.2 ± 16.51 ^{Mid}	0.057	
		4.14 ± 0.40 ^{In}	74.43 ± 8.77 ^{In}	0.056	
<i>Green mussel</i>	B	4.5	59.6	0.076	Barthelat et al., 2006
<i>Red abalone</i>	B	7.5	79	0.095	Leung et al., 2009
<i>Lamprotula fibrosa</i>	B	3.42	59.6	0.057	Sun et al., 2007
<i>Busycon carica</i>	G	5.6 ± 0.3 ^{Out}	89.1 ± 5.2 ^{Out}	0.063	Li et al., 2013
		5.8 ± 0.4 ^{Mid}	89.0 ± 7.1 ^{Mid}	0.065	
		5.7 ± 0.5 ^{In}	83.2 ± 7.3 ^{In}	0.069	
		4.9 ^T	89 ^T	0.055	
		4.7 ^L 4.4 ^P	99 ^L 101 ^P	0.047 0.044	
<i>Hemifusus tuba</i>	G	3.9 ± 0.3 ^{PE}	84 ± 5 ^{PE}	0.046	Zhao et al., 2010
		5.6 ± 0.2 ^{PA}	99 ± 3 ^{PA}	0.057	
<i>Strombus gigas</i>	G				Romana et al., 2013

B: bivalve, G: gastropod.

In: inner layer, Mid: middle layer, Out: outer layer.

T: transverse section, L: longitudinal section, P: plane section.

PE: perpendicular to the growth axis, PA: parallel to the growth axis.

0.05, which was similar to our results.

3.3. Permineralization mechanism

The skeleton of marine organisms is an intimate composition of organic matter and minerals. The composition undergoes permineralization after the death of the organism. The permineralization process occurs in sea water, which contains abundant minerals. After permineralization, the mollusk shell exhibited a slight decrease in organic matter content, a significant decrease in porosity, and increases in the thickness and area of aragonite platelets. These phenomena may be caused by three consecutive steps: biodegradation of the organic fraction, compaction of the aragonite platelets, and recrystallization of the aragonite crystals (Jannello et al., 2018). In the early stage of permineralization, the degradation phenomena of organic matter caused by mineral fluids in the sea result in the increased porosity in the mollusk shell skeleton. (Hedges et al., 1995). Owing to the degraded occluded

organics, many multisized holes were formed within the shells, which can act as channels that transport mineral fluids into the shell hard tissue and provide space for mineral precipitation between the primitive mineral units. Subsequently, the *J-Tridacna gigas* went through a compression processes as a result of lithostatic pressure under the sea. The lithostatic pressure caused a series of plastic deformations and aragonite plate amalgamations in the skeleton after losing organic matter. The aragonite plate amalgamated by growing laterally at the expense of neighboring fibers, so that the aragonite crystal volume increased, the porosity decreased, and a large fracture stress was required. The fracture stress can be expressed as follows:

$$\sigma_{crit} = \sqrt{2E\gamma^s/\pi c} \quad (3)$$

where σ_{crit} is the fracture stress, γ^s is the surface energy of the new fracture surface, E is the elastic modulus, and c is the half length of the crack. As the crack length decreased, the fracture stress (σ_{crit}) of *J-Tridacna gigas* was improved. Moreover, the strength of the crystal preferred orientation and the mechanical anisotropy decreased (Laura A. Casella et al., 2018). In addition, the composite and hierarchical structure of the shell provided strain-related driving forces and surface energy for recrystallization. Similarly, the cavities, voids, and holes produced by the degradation of organic matter also added to the driving force for recrystallization (L.A. Casella et al., 2018). Thus, the permineralization process of *J-Tridacna gigas* could result in coarsening of the aragonite platelets and a decrease in anisotropy accompanied by a significantly reduced porosity and increased hardness.

3.4. Failure behavior and failure mechanisms

To better understand the influence of permineralization after *Tridacna gigas* death on the damage features, a Vickers hardness test was applied to normal and *J-Tridacna gigas*, and their indentation morphologies are shown in Fig. 13a and b, respectively. Clearly, many microcracks can be observed around the *Tridacna gigas* indentation, which initiate around the indentation and propagate along the interfaces of the lamellae until being finally arrested by the interfaces. However, compared with the short cracks on the *Tridacna gigas*, the microcracks are longer and straighter on the *J-Tridacna gigas*, where the microcracks can spread more easily along the interfaces of the aragonite plate, as shown in Fig. 13b. This phenomenon indicated that the fracture toughness of *J-Tridacna gigas* was lower than that of *Tridacna gigas*, which is consistent with our research results, as shown in Fig. 8d. However, compared with geological aragonite, *J-Tridacna gigas* had a better fracture toughness because of its crossed-lamellar structure. The unique construction of the crossed-lamellar structure provides multiple complex interfaces at different levels of lamellae, which provide several energy dissipating mechanisms (Ji et al., 2017). The propagation of cracks, such as zig-zag paths, crack bridging, crack deflection, and platelet pull-out, improve the damage resistance (Jiao et al., 2016b). As shown in Fig. 13, two types of bridging were found on *J-Tridacna gigas* as the cracks mainly propagated along the interface of the lamellae. Uncracked-ligament bridges appeared on the propagation paths of cracks (as shown in Fig. 13c) along with crack deflection in the form of zig-zag paths, which illustrated the presence of substantial crack propagation resistance, as shown in Fig. 13d. In addition, aragonite platelets were left intact and acted as bridges to carry load that would otherwise be used to spread the cracks (Fig. 13e). Thus, crack bridging could absorb more energy to effectively prevent crack propagation and improve the fracture toughness of the shell. Moreover, many aragonite platelets were pulled out, as marked in Fig. 13f, again representing the large crack propagation resistance (Ji et al., 2019).

The observed crack deflection, crack bridging, and aragonite platelet pull-out in the complicated structures between macrolayers played a key role in strengthening and toughening the *J-Tridacna gigas*. These toughening failure mechanisms can also be observed in human bones,

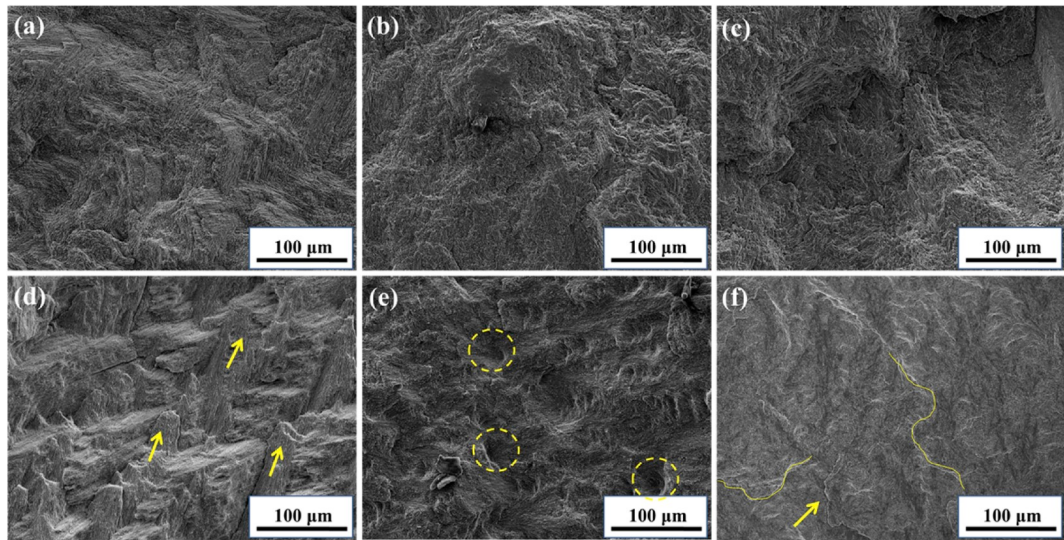


Fig. 11. SEM micrographs: fracture surfaces of the (a, d) parallel samples (surface C), (b, e) thickness samples (surface B), and (c, f) perpendicular samples (surface A) of jade and normal *Tridacna gigas*. The fracture surfaces of the samples were taken from the flexural tests.

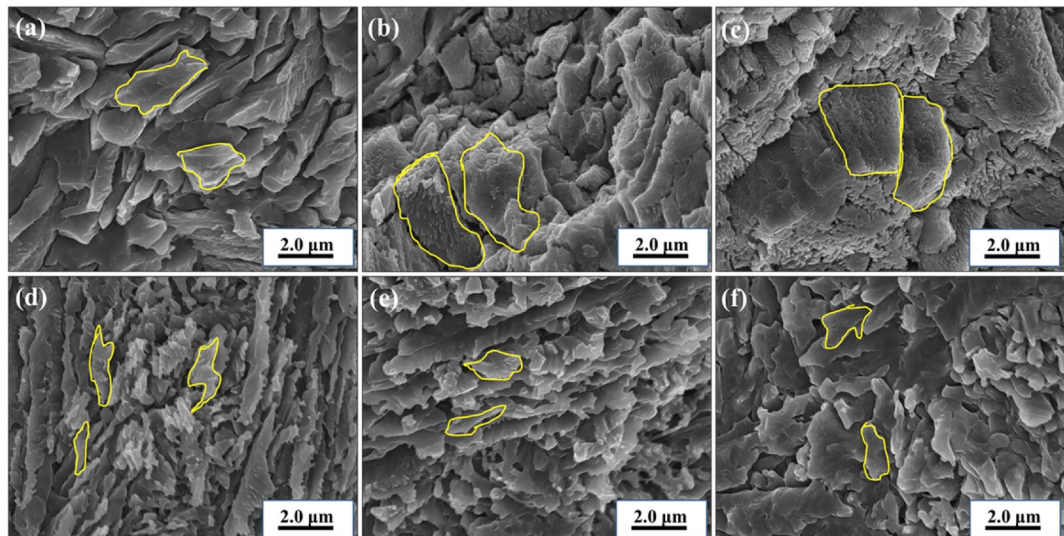


Fig. 12. High-magnification SEM micrographs: fracture surfaces of the (a, d) parallel samples (surface C), (b, e) thickness samples (surface B), and (c, f) perpendicular samples (surface A) of jade and normal *Tridacna gigas*. The fracture surfaces of the samples were taken from the flexural tests.

leatherback sea turtle shells, and alligator osteoderms.

4. Conclusion

In this work, the influence of permineralization on the compositions, microstructures, and mechanical properties of *Tridacna gigas* was systematically studied. Both jade and normal *Tridacna gigas* consisted of pure aragonite phase; however, the organic content of J-*Tridacna gigas* was half the weight percentage of that in *Tridacna gigas* and absorbed very little humidity. The hierarchical lamellar structure was observed in three hierarchies (lamellar, platelets, and rods), constructed by the highly aligned packing of aragonite nanorods, and some nanograins were distributed on the surface of the aragonite rods.

The relationship between microstructure and mechanical properties was investigated in jade and normal *Tridacna gigas*. The increased aragonite crystal size and the decreased organic matter content during permineralization played the most important roles in the mechanical properties. The mechanical properties of both samples were anisotropic.

However, the anisotropy of J-*Tridacna gigas* was not as noticeable as that of *Tridacna gigas*. The hardness and compressive strength of J-*Tridacna gigas* were higher than those of *Tridacna gigas* in the three orientations, which was also due to the soft matter loss and microstructure coarsening. The bending strength and fracture toughness of *Tridacna gigas*, especially in the samples cut parallel to the growth line, were much higher than those of J-*Tridacna gigas* due to the viscoelastic properties provided by the organic matter. Moreover, the permineralization mechanism of *Tridacna gigas* was proposed to comprise organic matter dissolution, aragonite rod compaction, and recrystallization. J-*Tridacna gigas* not only has high hardness and strength but also has toughening mechanisms, including crack deflection, mineral bridges, and aragonite platelet pull-out, because it is composed of complex hierarchical structures.

This study investigated the difference in microstructure and mechanical properties between J-*Tridacna gigas* and *Tridacna gigas*. The research results revealed the critical role of the organic contents between nanorods on the mechanical properties during permineralization.

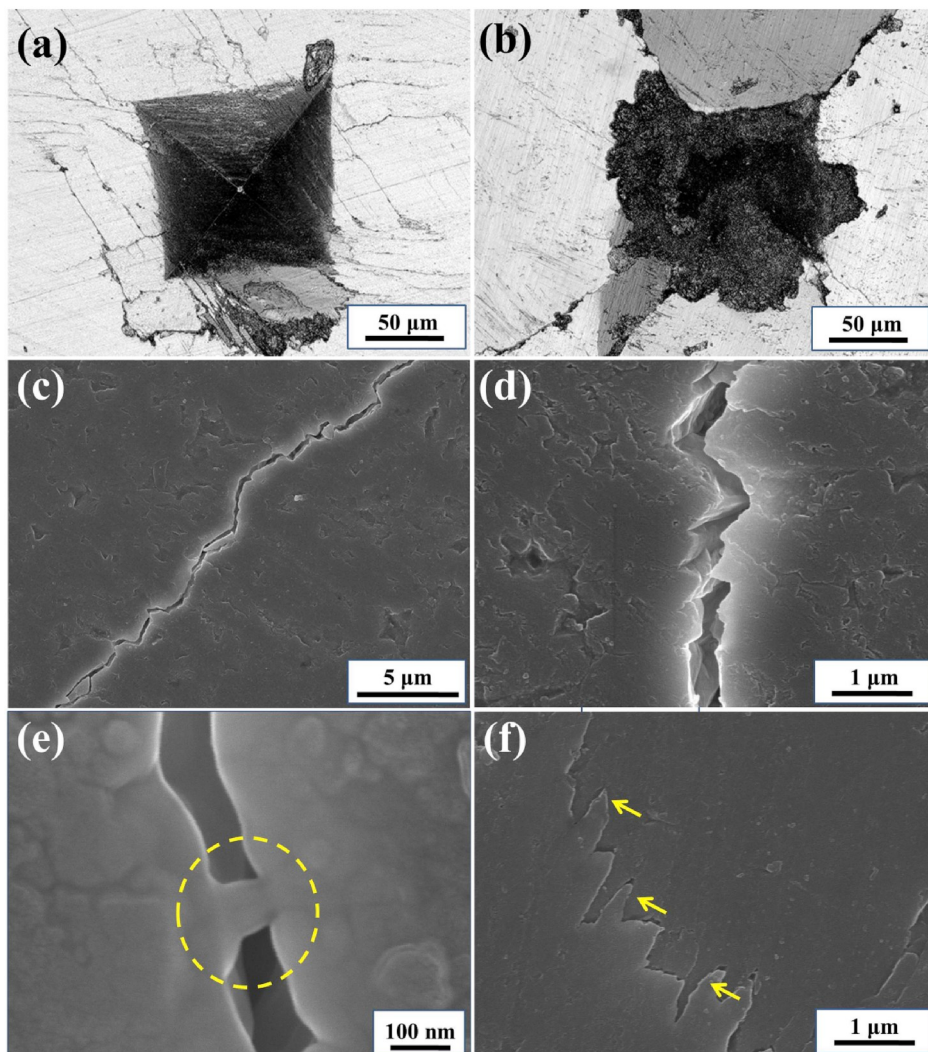


Fig. 13. Failure behavior images of jade and normal *Tridacna gigas* by Vickers hardness test. (a, b) Overall views of normal and J-*Tridacna gigas* after indentation. (c–f) Fracture micrographs of crack deflection, zig-zag paths, mineral bridge, and aragonite platelet pull-out after indentation of J-*Tridacna gigas*.

The findings in permineralization and toughening mechanisms of J-*Tridacna gigas* provide valuable insights into the microstructure design of hierarchical structures for bioinspired advanced materials with outstanding hardness and strength.

Declaration of competing interest

We declare that we do not have any commercial or associative interest that represents a conflict of interest in connection with the work submitted.

CRediT authorship contribution statement

Xue Hou: Data curation, Writing - original draft, Investigation. **Hui Yu:** Resources. **Zhenhao Hou:** Investigation. **Jianbao Li:** Conceptualization, Methodology. **Yongjun Chen:** Writing - review & editing. **Lijie Luo:** Resources. **Xianzhi Chen:** Investigation. **Wei Li:** Resources. **Huan Yang:** Investigation. **Wei Zeng:** Writing - review & editing.

Acknowledgments

The authors thank Mr. Qiangsen Li for his help in cutting the *Tridacna gigas* samples. This work is supported by the National Natural Science

Foundation of China (No. 51662006). The authors would like to thank Professor Wen Feng's research group for providing nanoindenter support.

Appendix A. Supplementary data

Supplementary data to this article can be found online at <https://doi.org/10.1016/j.jmbbm.2019.103609>.

References

- Addadi, L., Joester, D., Nudelman, F., Weiner, S., 2006. Mollusk shell formation: a source of new concepts for understanding biomineralization processes. *Chem. Eur. J.* 12, 980–987. <https://doi.org/10.1002/chem.200500980>.
- Agbaje, O.B.A., Thomas, D.E., McInerney, B.V., Molloy, M.P., Jacob, D.E., 2017. Organic macromolecules in shells of *Arctica islandica*: comparison with nacreopristmatic bivalve shells. *Mar. Biol.* 164 <https://doi.org/10.1007/s00227-017-3238-2>.
- Agbaje, O.B.A., Wirth, R., Morales, L.F.G., Shirai, K., Kosnik, M., Watanabe, T., Jacob, D. E., 2017. Architecture of crossed-lamellar bivalve shells: the southern giant clam (*Tridacna derasa*, Röding, 1798). *R. Soc. Open Sci.* 4, 170622. <https://doi.org/10.1098/rsos.170622>.
- Aizenberg, J., 2005. Skeleton of *euplectella* sp.: structural hierarchy from the nanoscale to the macroscale. *Science* 309, 275–278. <https://doi.org/10.1126/science.1112255>.
- Barthelat, F., Li, C.-M., Comi, C., Espinosa, H.D., 2006. Mechanical properties of nacre constituents and their impact on mechanical performance. *J. Mater. Res.* 21, 1977–1986. <https://doi.org/10.1557/jmr.2006.0239>.

- Bechtle, S., Ang, S.F., Schneider, G.A., 2010. On the mechanical properties of hierarchically structured biological materials. *Biomaterials* 31, 6378–6385. <https://doi.org/10.1016/j.biomaterials.2010.05.044>.
- Boufala, K., Ouenhenia, S., Betrancourt, D., Chicot, D., Belabbas, I., 2019. Microstructure analysis and mechanical properties by instrumented indentation of *Charonia lampas* lampas shell. *J. Mech. Behav. Biomed. Mater.* 89, 114–121. <https://doi.org/10.1016/j.jmbbm.2018.09.018>.
- Casella, L.A., Griesshaber, E., Yin, X., Ziegler, A., Mavromatis, V., Müller, D., Ritter, A.-C., Hippler, D., Harper, E.M., Dietzel, M., Immenhauser, A., Schöne, B.R., Angiolini, L., Schmahl, W.W., 2017. Experimental diagenesis: insights into aragonite to calcite transformation of *< i>Arctica islandica</i>* shells by hydrothermal treatment. *Biogeosciences* 14, 1461–1492. <https://doi.org/10.5194/bg-14-1461-2017>.
- Dunlop, J.W.C., Fratzl, P., 2013. Multilevel architectures in natural materials. *Scr. Mater.* 68, 8–12. <https://doi.org/10.1016/j.scriptamat.2012.05.045>.
- Fleischli, F.D., Dietiker, M., Borgia, C., Spolenak, R., 2008. The influence of internal length scales on mechanical properties in natural nanocomposites: a comparative study on inner layers of seashells. *Acta Biomater.* 4, 1694–1706. <https://doi.org/10.1016/j.actbio.2008.05.029>.
- Gannon, M.E., Pérez-Huerta, A., Aharon, P., Street, S.C., 2017. A biomineralization study of the Indo-Pacific giant clam *Tridacna gigas*. *Coral Reefs* 36, 503–517. <https://doi.org/10.1007/s00338-016-1538-5>.
- Hedges, R.E.M., Millard, A.R., Pike, A.W.G., 1995. Measurements and Relationships of Diagenetic Alteration of Bone from Three Archaeological Sites. *J. Archaeol. Sci* 201–209. <https://doi.org/10.1006/jasc.1995.0022>.
- Jannello, J.M., Maniel, I.J., Previtera, E., Fuente, M.S., 2018. *Linderochelys rinconensis* (Testudines: Pan-Chelidae) from the Upper Cretaceous of northern Patagonia: New insights from shell bone histology, morphology and diagenetic implications. *Cretac. Res* 83, 47–61. <https://doi.org/10.1016/j.cretres.2017.05.011>.
- Ji, B., Gao, H., 2004. Mechanical properties of nanostructure of biological materials. *J. Mech. Phys. Solids* 52, 1963–1990. <https://doi.org/10.1016/j.jmps.2004.03.006>.
- Ji, H., Li, X., Chen, D., 2017. *Cymbiola nobilis* shell: toughening mechanisms in a crossed-lamellar structure. *Sci. Rep.* 7 <https://doi.org/10.1038/srep40043>.
- Ji, H.-M., Jiang, Y., Yang, W., Zhang, G.-P., Li, X.-W., 2015. Biological self-arrangement of fiber like aragonite and its effect on mechanical behavior of *Veined rapa whelk* shell. *J. Am. Ceram. Soc.* 98, 3319–3325. <https://doi.org/10.1111/jace.13733>.
- Ji, H.-M., Li, X.W., Chen, D.L., 2019. Crack initiation and growth in a special quasi-sandwich crossed-lamellar structure in *Cymbiola nobilis* seashell. *J. Mech. Behav. Biomed. Mater.* 90, 104–112. <https://doi.org/10.1016/j.jmbbm.2018.09.049>.
- Ji, H.-M., Zhang, W.Q., Li, X.W., 2014. Fractal analysis of microstructure-related indentation toughness of *Clinocardium californiense* shell. *Ceram. Int.* 40, 7627–7631. <https://doi.org/10.1016/j.ceramint.2013.12.035>.
- Ji, H.-M., Zhang, W.Q., Wang, X., Li, X.-W., 2015. Three-point bending fracture behavior of single oriented crossed-lamellar structure in *Scapharca broughtonii* shell. *Materials* 8, 6154–6162. <https://doi.org/10.3390/ma8095298>.
- Jiao, D., Liu, Z.Q., Qu, R.T., Zhang, Z.F., 2016. Anisotropic mechanical behaviors and their structural dependences of crossed-lamellar structure in a bivalve shell. *Mater. Sci. Eng. C* 59, 828–837. <https://doi.org/10.1016/j.msec.2015.11.003>.
- Jiao, D., Liu, Z.Q., Zhu, Y.K., Weng, Z.Y., Zhang, Z.F., 2016. Mechanical behavior of mother-of-pearl and pearl with flat and spherical laminations. *Mater. Sci. Eng. C* 68, 9–17. <https://doi.org/10.1016/j.msec.2016.05.089>.
- Katti, K.S., Mohanty, B., Katti, D.R., 2006. Nanomechanical properties of nacre. *J. Mater. Res* 21, 1237–1242. <https://doi.org/10.1557/jmr.2006.0147>.
- Labonte, D., Lenz, A.-K., Oyen, M.L., 2017. On the relationship between indentation hardness and modulus, and the damage resistance of biological materials. *Acta Biomater.* 57, 373–383. <https://doi.org/10.1016/j.actbio.2017.05.034>.
- Leung, H.M., Sinha, S.K., 2009. Scratch and indentation tests on seashells. *Tribol. Int.* 42, 40–49. <https://doi.org/10.1016/j.triboint.2008.05.015>.
- Li, L., Ortiz, C., 2014. Pervasive nanoscale deformation twinning as a catalyst for efficient energy dissipation in a bioceramic armour. *Nat. Mater.* 13, 501–507. <https://doi.org/10.1038/nmat3920>.
- Li, H.Z., Xu, Z.H., Li, X.D., 2013. Multiscale hierarchical assembly strategy and mechanical prowess in conch shells (*Busycon carica*). *J. Struct. Biol* 184, 409–416. <https://doi.org/10.1016/j.jsb.2013.10.011>.
- Lin, A.Y.M., Meyers, M.A., Vecchio, K.S., 2006. Mechanical properties and structure of *Strombus gigas*, *Tridacna gigas*, and *Haliotis rufescens* sea shells: a comparative study. *Mater. Sci. Eng. C* 26, 1380–1389. <https://doi.org/10.1016/j.msec.2005.08.016>.
- Lu, J., Cong, X., Li, Y., Hao, Y., Wang, C., 2018. Scalable recycling of oyster shells into high purity calcite powders by the mechanochemical and hydrothermal treatments. *J. Clean. Prod.* 172, 1978–1985. <https://doi.org/10.1016/j.jclepro.2017.11.228>.
- Marin, F., 2012. The formation and mineralization of mollusk shell. *Front. Biosci. S4*, 1099–1125. <https://doi.org/10.2741/s321>.
- Meyers, M.A., Chen, P.-Y., Lin, A.Y.-M., Seki, Y., 2008. Biological materials: structure and mechanical properties. *Prog. Mater. Sci.* 53, 1–206. <https://doi.org/10.1016/j.pmatsci.2007.05.002>.
- Mishra, N., Kandasubramanian, B., 2018. Biomimetic design of artificial materials inspired by iridescent nacre structure and its growth mechanism. *Polym. Plast. Technol. Eng.* 57, 1592–1606. <https://doi.org/10.1080/03602559.2017.1326139>.
- Mohamed, M., Rashidi, N.A., Yusup, S., Teong, L.K., Rashid, U., Ali, R.M., 2012. Effects of experimental variables on conversion of cockle shell to calcium oxide using thermal gravimetric analysis. *J. Clean. Prod.* 37, 394–397. <https://doi.org/10.1016/j.jclepro.2012.07.050>.
- Mu, G., Duan, F., Zhang, G., Li, X., Ding, X., Zhang, L., 2018. Microstructure and mechanical property of *Ruditapes philippinarum* shell. *J. Mech. Behav. Biomed. Mater.* 85, 209–217. <https://doi.org/10.1016/j.jmbbm.2018.06.012>.
- Pérez-Huerta, A., Coronado, I., Hegna, T.A., 2018. Understanding biomineralization in the fossil record. *Earth Sci. Rev.* 179, 95–122. <https://doi.org/10.1016/j.earscirev.2018.02.015>.
- Perrin, C., Smith, D.C., 2007. Earliest steps of diagenesis in living scleractinian corals: evidence from ultrastructural pattern and Raman spectroscopy. *J. Sediment. Res.* 77, 495–507. <https://doi.org/10.2110/jsr.2007.051>.
- Pokroy, B., Demensky, V., Zolotoyabko, E., 2009. Nacre in mollusk shells as a multilayered structure with strain gradient. *Adv. Funct. Mater.* 19, 1054–1059. <https://doi.org/10.1002/adfm.200801201>.
- Ritter, A.-C., Mavromatis, V., Dietzel, M., Kwiecien, O., Wiethoff, F., Griesshaber, E., Casella, L.A., Schmahl, W.W., Koelen, J., Neuser, R.D., Leis, A., Buhl, D., Niedermayr, A., Breitenbach, S.F.M., Bernasconi, S.M., Immenhauser, A., 2017. Exploring the impact of diagenesis on (isotope) geochemical and microstructural alteration features in biogenic aragonite. *Sedimentology* 64, 1354–1380. <https://doi.org/10.1111/sed.12356>.
- Rodríguez, S., Brañez, L.E., Torres, F.G., Fernández-García, M., López, D., 2017. Revisiting the role of calcite in *Spondylus crassisquama* shell. *Bioinspired, Biomimetic Nanobiomaterials* 6, 151–160. <https://doi.org/10.1680/jbibn.16.00032>.
- Romana, L., Thomas, P., Mansot, J.L., Merrifield, M., Bercion, Y., Aranda, D.A., 2013. Use of nanoindentation technique for a better understanding of the fracture toughness of *Strombus gigas* conch shell. *Mater. Charact.* 76, 55–68. <https://doi.org/10.1016/j.matchar.2012.11.010>.
- Schoeppeler, V., Gránásy, L., Reich, E., Poulsen, N., Kloe, R., Cook, P., Rack, A., Puszta, T., Zlotnikov, I., 2018. Biomineralization as a paradigm of directional solidification: physical model for Molluscan shell ultrastructural morphogenesis. *Adv. Mater.* 30, 1803855. <https://doi.org/10.1002/adma.201803855>.
- Seiphori, A., Whittle, A.J., Krakowiak, K.J., Einstein, H.H., 2017. Insights into diagenesis and pore structure of opalinus shale through comparative studies of natural and reconstituted materials. *Clay Clay Miner.* 65, 135–153. <https://doi.org/10.1346/CCMN.2017.064055>.
- Sun, J., Bhushan, B., 2012. Hierarchical structure and mechanical properties of nacre: a review. *RSC Adv* 2, 7617. <https://doi.org/10.1039/c2ra20218b>.
- Toffolo, M., Regev, L., Dubernet, S., Lefrais, Y., Boaretto, E., 2019. FTIR-based crystallinity assessment of aragonite–calcite mixtures in archaeological lime binders altered by diagenesis. *Minerals* 9, 121. <https://doi.org/10.3390/min9020121>.
- Wang, R.Z., Suo, Z., Evans, A.G., Yao, N., Aksay, I.A., 2001. Deformation mechanisms in nacre. *J. Mater. Res.* 16, 2485–2493. <https://doi.org/10.1557/JMR.2001.0340>.
- Wegst, U.G.K., Bai, H., Saiz, E., Tomsia, A.P., Ritchie, R.O., 2015. Bioinspired structural materials. *Nat. Mater.* 14, 23–36. <https://doi.org/10.1038/nmat4089>.
- Weiner, S., 2008. Biomineralization: a structural perspective. *J. Struct. Biol.* 163, 229–234. <https://doi.org/10.1016/j.jsb.2008.02.001>.
- Yang, W., Kashani, N., Li, X.-W., Zhang, G.-P., Meyers, M.A., 2011. Structural characterization and mechanical behavior of a bivalve shell (*Saxidomus purpuratus*). *Mater. Sci. Eng. C* 31, 724–729. <https://doi.org/10.1016/j.msec.2010.10.003>.
- Yang, W., Zhang, G., Liu, H., Li, X., 2011. Microstructural characterization and hardness behavior of a biological *Saxidomus purpuratus* shell. *J. Mater. Sci. Technol.* 27, 139–146. [https://doi.org/10.1016/S1005-0302\(11\)60039-X](https://doi.org/10.1016/S1005-0302(11)60039-X).
- Yang, W., Zhang, G.P., Zhu, X.F., Li, X.W., Meyers, M.A., 2011. Structure and mechanical properties of *Saxidomus purpuratus* biological shells. *J. Mech. Behav. Biomed. Mater.* 4, 1514–1530. <https://doi.org/10.1016/j.jmbbm.2011.05.021>.
- Zhang, G., Xu, J., 2013. From colloidal nanoparticles to a single crystal: new insights into the formation of nacre's aragonite tablets. *J. Struct. Biol.* 182, 36–43. <https://doi.org/10.1016/j.jsb.2013.01.010>.
- Zhang, Y., Heim, F.M., Bartlett, J.L., Song, N., Isheim, D., Li, X., 2019. Bioinspired, graphene-enabled Ni composites with high strength and toughness. *Sci. Adv.* 5, eaav5577. <https://doi.org/10.1126/sciadv.aav5577>.
- Zhao, J., Chen, C., Liang, Y., Wang, J., 2010. Mechanical properties and structure of *Haliotis discus hannai* Ino and *Hemifusus tuba* conch shells: a comparative study. *Acta Mech. Sin* 26, 21–25. <https://doi.org/10.1007/s10409-009-0308-9>.